Cramér-Rao Bounds for Wavelet Frequency Estimates

R.A. Scheper
Tactical Electronic Warfare Division

A. Teolis
AIMS, Inc.

Introduction: The problem of information extraction from noisy frequency-modulated (FM) signals is of fundamental importance in a variety of Naval applications including communication, radar, and electronic surveillance. As modulation techniques become more complex and signal bandwidths move into the GHz range, extraction algorithms must become ever more sophisticated and yet remain computationally tractable so as to process incoming signals at or near real time. We consider the well-studied problem of instantaneous frequency (IF) estimation from a novel perspective in the wavelet transform domain.

A very first step in the development of algorithms is to identify the fundamental limits of their performance. In estimation applications, this usually translates into determining a fundamental limit on the variance of the estimator. For unbiased estimators, this limit is the Cramér-Rao bound (CRB). In establishing the minimum attainable variance for any estimate, the CRB provides a standard against which to measure estimation algorithm performance in the presence of noise.

Wavelet-Based IF Estimation: Wavelet transforms offer themselves as powerful tools for the analysis of FM signals. A wavelet transform takes a one-dimensional signal of time into a two-dimensional signal of time and frequency. The result is a joint time-frequency (TF) distribution that describes the evolution of the signal frequency content over time. Figure 1 depicts a wavelet filter bank and its response to a linear chirp signal. Judicious choice of the transform parameters yields TF distributions that tend to concentrate the signal energy along the frequency axis at or near the IF while simultaneously dispersing the noise energy uniformly. As such, they are inherently noise-tolerant and provide a basis for robust parameter estimation techniques.

Both signal and noise are modeled under the wavelet transform to provide an analytical relationship between the parameters of interest and the wavelet transform of the signal. Figure 2 shows the response of a wavelet filter bank to a noiseless fixed frequency sinusoid (left) and the same signal in noise with a 10 dB signal-to-noise ratio (right). An asymptotic approximation is developed for a wavelet transform of an FM signal to yield a transform model. This model explicitly depends on the key parameters

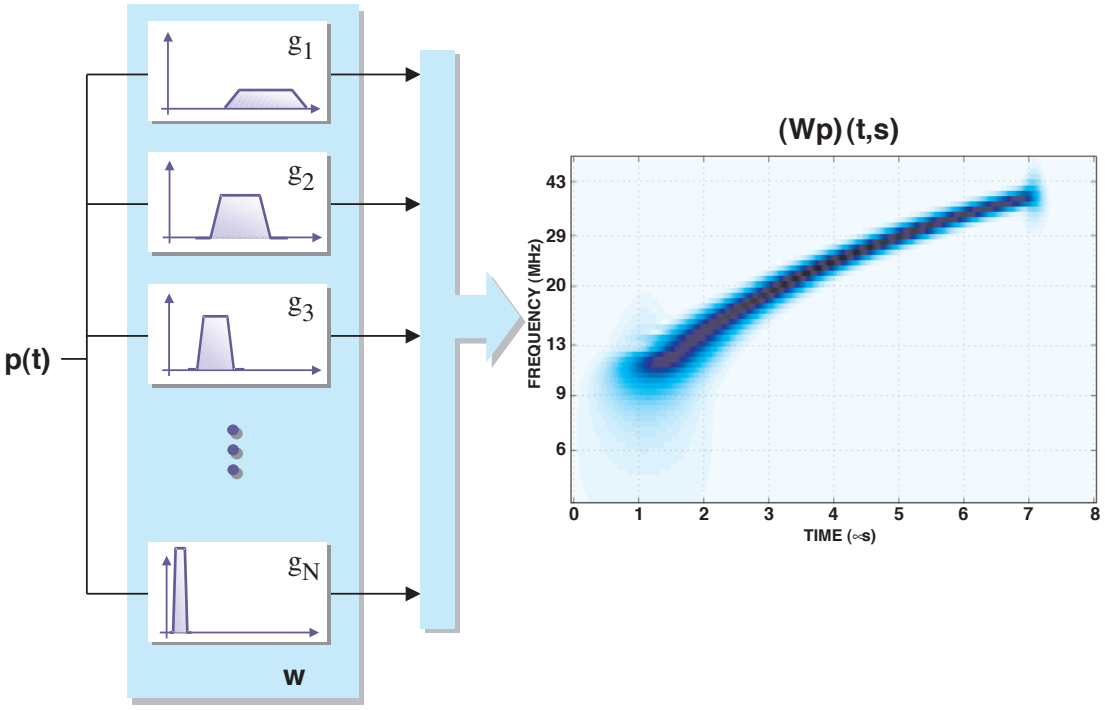

FIGURE 1
A wavelet filter bank and its response to an input signal with a linear FM (chirp).

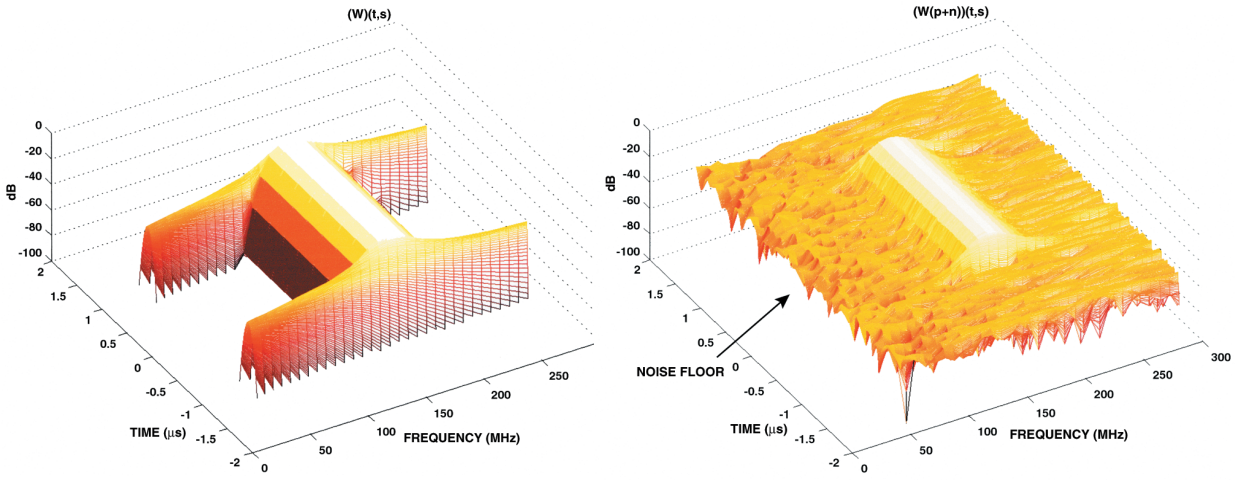

FIGURE 2
Time-frequency distributions associated with a fixed-frequency sinusoidal pulse: (left) distribution for signal only, and (right) distribution for signal plus noise.

of signal amplitude, signal phase, signal instantaneous frequency, and noise level. Fitting the model to the observed wavelet output provides the IF estimation mechanism. Figure 3 shows the model matching procedure for IF estimation; similar estimation procedures are possible for the other parameters.

Discussion: Obtaining simple transform approximation formulas is the key for developing fast and conceptually simple algorithms for estimating signal IF (and other parameters). Moreover, a model approximation of a given wavelet transform can provide the means to assess the performance of a particular algorithm when applied to noisy data. Some feasible tests include: comparisons of obtainable parameter variances between candidate algorithms for a given transform; specific comparisons of algorithm performance to the parent transform CRBs; comparisons of CRBs between different transforms; sensitivity of a given transform CRB to input parameters; and comparison of a given transform CRB to other extraction methods (e.g., polynomial phase model). In all, asymptotic approximations to wavelet transforms provide a good framework for both the development and analysis of IF estimation algorithms.

Summary: We exploit the property of the wavelet transform to concentrate signal energy along its FM trajectory in the wavelet domain to simultaneously achieve several objectives. These are (a) to develop an integral approximation of the wavelet transform; (b) to use the approximation to develop computational algorithms for IF estimation; and (c) to use the approximation to obtain the CRB of the IF estimate.

[Sponsored by NRL]

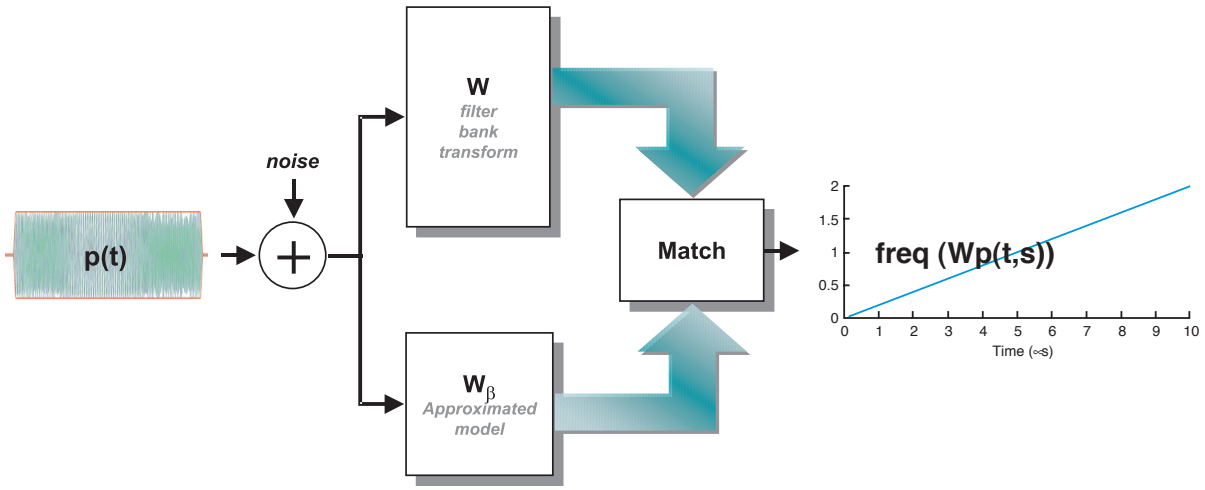

FIGURE 3
Estimation of signal IF via transform matching technique using a wavelet filter bank.

Spirals and Sea Surface Dynamics

C.Y. Shen and T.E. Evans
Remote Sensing Division

Introduction: Space flights and satellite-borne sensors have enabled surface features of the ocean to be observed in their entirety, many for the first time. The "spiral" of ~10 km diameter is one such feature discovered from space (Fig. 4) and, by far, is perhaps the most intriguing. Not only is its presence widespread, but its rotation is surprisingly distinct—cyclonic in the northern hemisphere and anticyclonic in the southern hemisphere. Since the spiral feature is made visible by slick lines wound up by the surface current, its occurrence suggests that some previously unrecognized processes are active near the sea surface. One possibility that has been considered is that the slick lines arise from surfactants concentrated along a converging density front and that their spiral shape is induced by eddies formed through flow instability along this front, which typically contains excess cyclonic or anticyclonic vorticity in the northern or southern hemisphere, respectively.[1] Although this explanation is plausible, evidence such as that shown in Fig. 4 suggests that many slick lines and spirals may have formed in situ, unrelated to the frontal convergence process. This process would have compressed multiple slick lines and would have produced spirals aligned along the convergence, none of which is apparent in the figure. On the other hand, a different process, known as "inertial" instability, can arise naturally in near-surface currents, with horizontal shears varying on a 10-km or less scale. Through three-dimensional computer modeling, we have shown that this instability can lead directly to the formation of slick lines and spirals, without the restrictive frontal preconditioning. Thus, it potentially can be a significant process near the sea surface, given the widespread occurrence of slick lines and spirals.

Inertial Instability: For a parallel shear current, the condition for the onset of inertial instability requires the sum of the horizontal current shear $\partial V/\partial x$ and twice the Earth's rotational frequency 2ω to be negative, viz., $\partial V/\partial x + 2\omega < 0$; here, V is the rectilinear current velocity directed perpendicularly to the across-stream coordinate x in a right-handed rectangular coordinate system. The onset of this instability is akin to the centrifugal instability that occurs in a rotating fluid body when the balance between the internal centrifugal force and pressure gradient force is disrupted by a local change of fluid rotation, a role played by $\partial V/\partial x$ on the rotating Earth. Thus, in the northern hemisphere, the inertially unstable currents

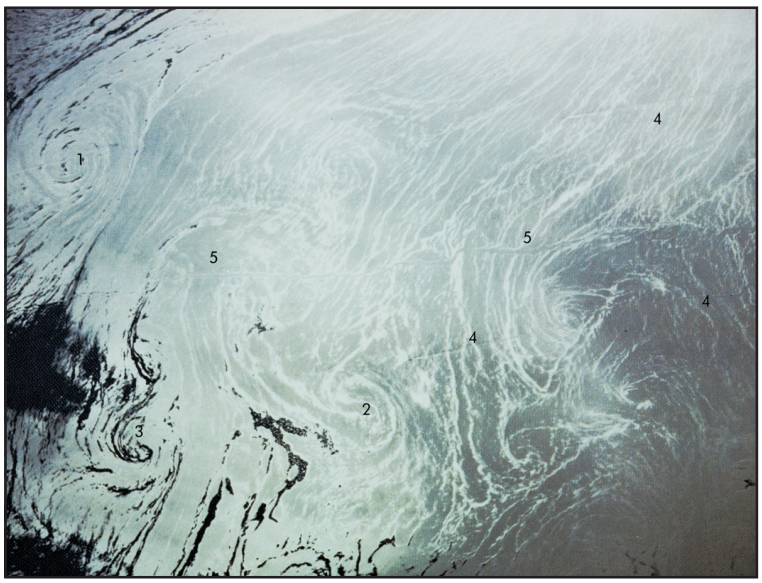

FIGURE 4
Sun-glint photograph of the central Mediterranean Sea taken from the Space Shuttle in 1984. Area covered (cropped from the original published photo) is ~150 km on each side. The bright bands are naturally occurring slicks. Numbers 1, 2, and 3 identify three of the several spirals visible on the sea surface. Some ship wakes are also visible on the surface and are indicated by numbers 4 and 5. (Courtesy of National Aeronautics and Space Administration, *Oceanography from Space*, 1986)

are those with $\partial V/\partial x < 0$ and $|\partial V/\partial x| > 2\omega$, since $\omega > 0$ with respect to a right-handed coordinate system in the northern hemisphere. The opposite holds in the southern hemisphere where $\omega < 0$. Noting this sign difference, it suffices to describe the northern hemisphere case.

Vortex and Spiral Generation: Figure 5 shows the unfolding instability in the ocean surface mixed layer, assumed 30-m depth, calculated with a nonlinear hydrodynamic model, with $V = (30\ \text{cm/s})\sin(2\pi x/10\ \text{km})$ and $\omega = 3.5 \times 10^{-5}$/s, the local normal component around mid-latitudes. The instability acts normal to V in an across-current vertical section. In less than a day, the distortion of V in the inertially unstable region ($\partial V/\partial x < 0$) has become quite pronounced. As the instability continues, an increasingly larger portion of V including the inertially stable region ($dV/dx > 0$) is affected. By day 2.37, the unstable motion has filled the entire width of the current. By this time, it is significant to note that the anticyclonic shear has been greatly reduced by its conversion to across-stream motion and is no longer inertially unstable. Simultaneously, the stable cyclonic shear region has become narrow and the shear has been enhanced by the across-stream motion.[2] Thus, the process has led to the emergence of a current structure that is inertially stable overall but strongly asymmetrical, with cyclonic shear favored.

Once the narrow, strongly cyclonic shear region emerges, the stage is set for the formation of the cyclonic eddy and spiral. Figure 6 shows the model sea surface at day 2.54. For better viewing, the cyclonic shear region has been shifted to the center of the plot. The velocity vector plots show that the center of the enhanced cyclonic shear zone rapidly develops a bulge in which a closed cyclonic circulation forms and evolves into a nearly circular eddy. This development can be explained in terms of the well-known shear flow instability process, in which concentrated shear induces its own across-stream circulation. Shown below each velocity vector plot is the simulated "surfactant" tracer field evolved from an initially uniform distribution. The bright bands or lines are high surfactant concentrations produced by the surface flow convergence occurred during the inertial instability. These plots show how the central bright "slick" line is eventually wound up by the vortical

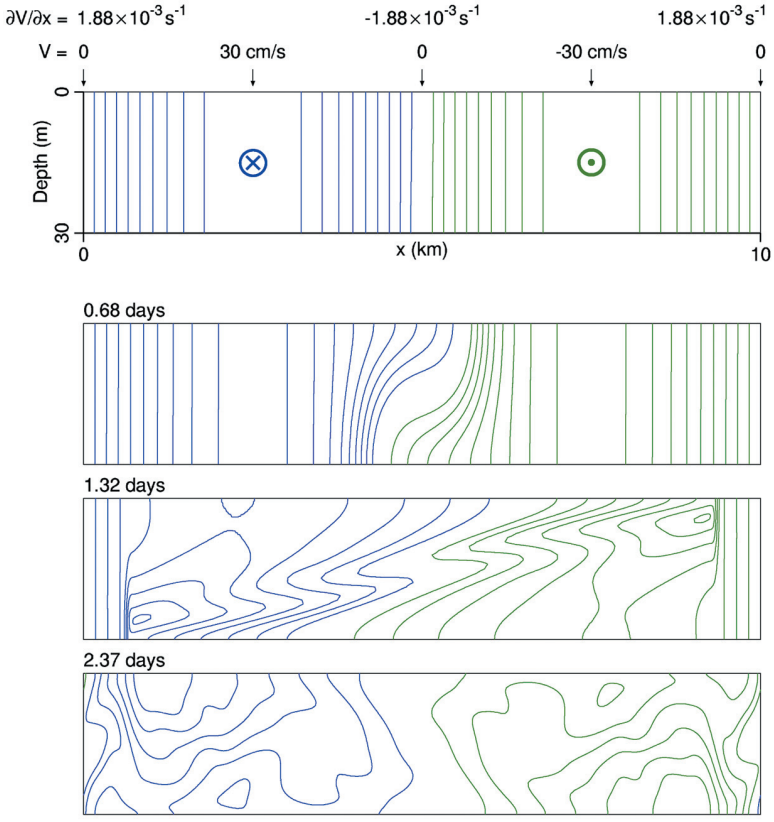

FIGURE 5
Vertical section of current velocity V. Positive V (blue) into the page and negative V (green) out of page. The contour interval is 3 cm/s. (Adapted from Ref. 2.)

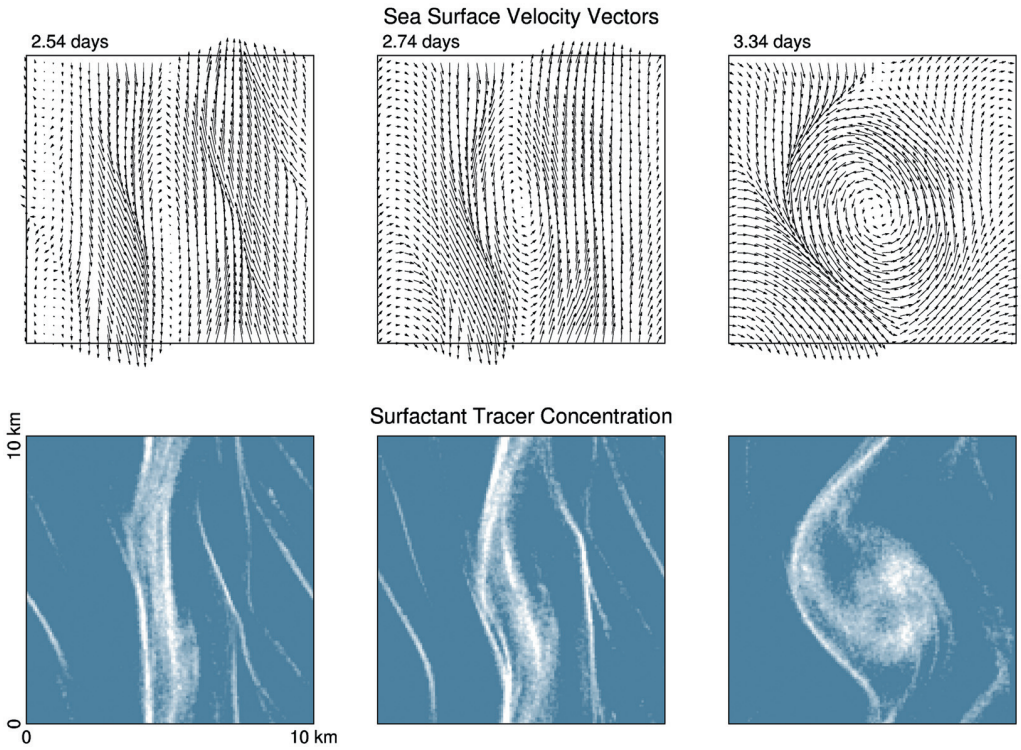

FIGURE 6
Plan view of the model sea surface. The longest velocity vector is 19.6 cm/s. The relative concentration of "surfactant" tracer is shown, with the upper 10% in white and lower 2% in blue.

motion into a cyclonic spiral. These simulated patterns of slicks are thus similar to those in Fig. 4. The formation of a spiral from inertial instability is reproducible by using initial velocity distributions that differ from the case illustrated here, and the process is presently being quantified.

Summary: Space-borne remote sensing is relied upon today by the Navy as well as the civilian community for gathering up-to-date information about the ocean environment. To be able to extract useful information from remote sensing requires proper interpretation of what has been observed. The intriguing spiral feature discovered through remote sensing has been shown by our modeling study to likely be a product of near-surface current inertial instability. NRL is planning a series of field experiments to measure the spiral and associated slick lines so that a full understanding of this feature can be achieved.

[Sponsored by ONR]

References

[1] W. Munk, L. Armi, K. Fischer, and F. Zachariasen, "Spirals on the Sea," *Proc. Roy. Soc. Lond.* A **456**, 1217-1280 (2000).
[2] C.Y. Shen and T.E. Evans, "Inertial Instability of Large Rossby Number Horizontal Shear Flows in a Thin Homogeneous Layer," *Dyn. Atmos. Oceans* **26**, 185-208 (1998).

The Physics of Fine-Scale Remote Sensing of the Air-Sea Interface

M.A. Sletten, G.B. Smith, J.V. Toporkov, and R.A. Handler
Remote Sensing Division

X. Liu and J.H. Duncan
University of Maryland

Introduction: For a wide range of applications—from improved weather forecasting to Naval operations—the need exists to extract quantitative information from remotely sensed imagery of the sea. NRL's Remote Sensing Division is pursuing an integrated set of numerical and experimental investigations designed to understand the physics of radar and infrared (IR) remote sensing of the many small-scale surface features that contribute to the remotely sensed signal. These features include breaking waves, parasitic capillary waves, and shear-driven instabilities.

Ultra-Fine-Scale Radar Scattering from Breaking Waves: When viewed with a radar operating at a low grazing (high incidence) angle, breaking waves can produce a significant portion of the

total backscatter generated by the sea surface. Thus these surface features are of great interest to the marine remote sensing community. To further our understanding of the role that breaking waves play in radar remote sensing, NRL and University of Maryland researchers have recently conducted a laboratory investigation in which the ultrahigh-resolution radar backscatter produced by evolving breaking waves was collected simultaneously with wave-height profiles provided by a high-speed digital camera. This data set allows both the wave surface and the radar backscatter it produces to be studied in unprecedented detail.

Figure 7 shows an evolving breaking wave and the radar backscatter it produces. The optical image, Fig. 7(a), shows the surface profile of the wave at an instant in time, as collected by a high-speed digital camera. In Fig. 7(b), range scans of the corresponding radar backscatter envelope, collected by an ultrahigh-resolution instrumentation radar developed by NRL, are presented for both vertical polarization (VV, upper panel) and horizontal polarization (HH, lower panel). Both the optical and radar data are single frames extracted from time sequences that document the evolution of the dynamic surface and its radar echo. This combination of dual-polarized, ultrahigh-resolution radar and simultaneous, high-speed optical imagery allows unambiguous identification of the scattering centers. When used in conjunction with electromagnetic modeling, the associated scattering mechanisms can also be identified.

Radar scattering from breaking waves is also the subject of numerical modeling studies. Figure 8(a) shows the surface profile of an evolving breaker at an instant in time, as calculated using a numerical implementation of the Navier-Stokes equations developed by NRL. Figure 8(b) displays the simulated radar Doppler spectrum produced by this wave (over its entire lifetime) at a grazing angle of 10 deg and a radar center frequency of 30 GHz. This spectrum was computed by NRL researchers using a numerical solution of the electromagnetic scattering equations in conjunction with Monte-Carlo techniques.[1] The large peak near 90 Hz is caused by surface roughness that is bound to and moves with the crest of the breaking wave. The smaller peak near 40 Hz is caused by small-scale roughness that is advected by the underlying orbital-wave currents. The Doppler spectrum is of fundamental importance in synthetic aperture radar-based techniques designed to measure ocean surface currents. These NRL studies promise to improve these techniques and extend them into the low-grazing angle regime by identifying the breaking wave contribution.

High-Resolution IR Imaging of an Air-Water Interface: NRL researchers are also involved in understanding the thermal properties and hydrodynamic structure of the air-sea interface.[2] As wind blows across the interface, the surface is cooled and a very thin layer, often called the *cool skin* of the ocean surface, is formed. This layer is on the order

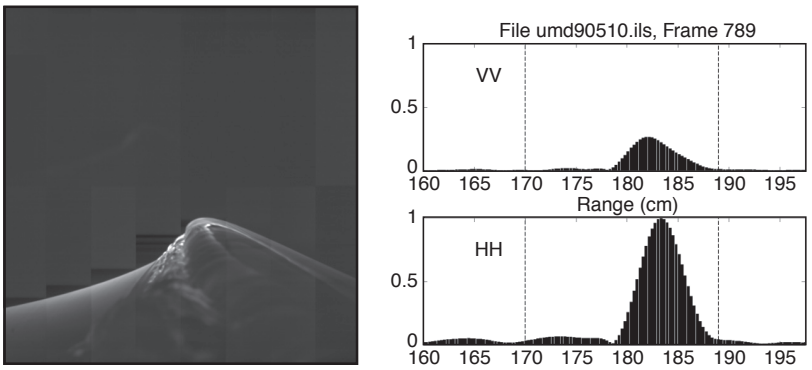

FIGURE 7
(a) High-speed photograph of the crest of an evolving breaking wave. The curved line separating the upper and lower sections of the photograph is the surface of the water. The wave has just begun to break and produce small-scale roughness on its forward face, just in front of the crest. (b) Magnitude of the radar backscatter produced by the breaking wave plotted vs range (upper panel: vertically polarized backscatter; lower panel: horizontally polarized). The vertical, dotted lines coincide with the left and right boundaries of the photograph field of view. The strong radar echoes are generated by the small-scale roughness just in front of the wave crest.

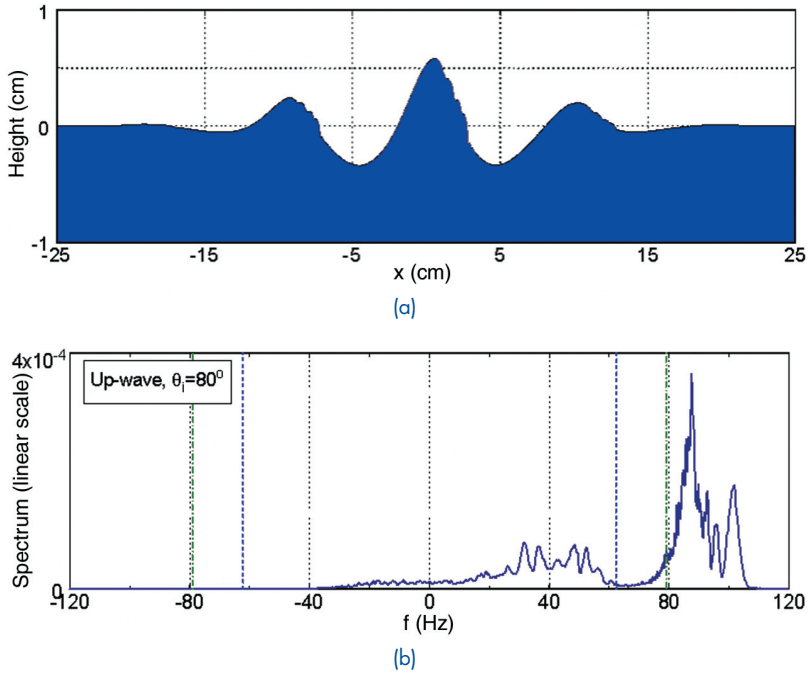

FIGURE 8
(a) Surface profile of an evolving breaking wave at a single instant in time, generated by a numerical solution to the Navier-Stokes equations. Wave propagation is from left to right. (b) Simulated radar Doppler spectrum at a frequency of 30 GHz for the breaking wave shown in (a). The strong peak near 90 Hz is produced by small-scale roughness bound to the wave crest, while the peak near 40 Hz is produced by freely propagating waves that are advected by the underlying orbital wave currents.

of a few millimeters in thickness and gives rise to an ocean surface temperature that is 0.1 to 0.5 K cooler than the subsurface fluid. An understanding of the physics associated with the nature of this cool skin is of considerable importance in the interpretation of satellite sea surface temperature (SST) imagery and in the development of improved heat flux models.

Figure 9 shows images of an air-water interface collected at the wind-wave facility at the University of Delaware by using a high-resolution IR camera with a temperature resolution of 0.02 K. The camera was mounted looking straight down at the water surface, which was driven by wind generated by a blower. In Fig. 9(a), where the wind speed was 2 ms^{-1}, it is evident that the cool skin has a well-defined structure made up of regions of warm fluid (bright regions) and cool dark streaks. These streaks are formed by a complex shear-induced hydrodynamic instability that have been shown to have a characteristic width $\lambda^+ = 100\, l^+$, where $l^+ = \nu/u^*$, ν is the kinematic viscosity of water, $u^* = (\tau/\rho)^{1/2}$, τ is the surface shear stress, and ρ is the water density. At 4 ms^{-1}, surface waves generate rapidly and sometimes form small-scale breaking events that appear as warm regions of homogeneous turbulence (Fig. 9(b)). By using companion numerical simulations of these phenomena, NRL researchers have recently developed new models that predict the heat flux at the air-sea interface for low wind speeds.

Summary: NRL is engaged in a series of experimental and numerical investigations into the remotely sensed signatures of small-scale ocean surface features. In future work, the IR and radar methods described here will be combined to provide new and unique insights into air-sea interfacial physics.

[Sponsored by NRL and ONR]

References

[1] J.V. Toporkov and G.S. Brown, "Numerical Simulations of Scattering from Time-Varying, Randomly Rough Surfaces," *IEEE Trans. Geosci. Remote Sensing*, **38** (4), 1616-1625 (2000).
[2] R.A. Hander, G.B. Smith, and R.I. Leighton, "The Thermal Atructure of an Air-Water Interface at Low Wind Speeds," *Tellus*, **53A**, 233-244 (2001).

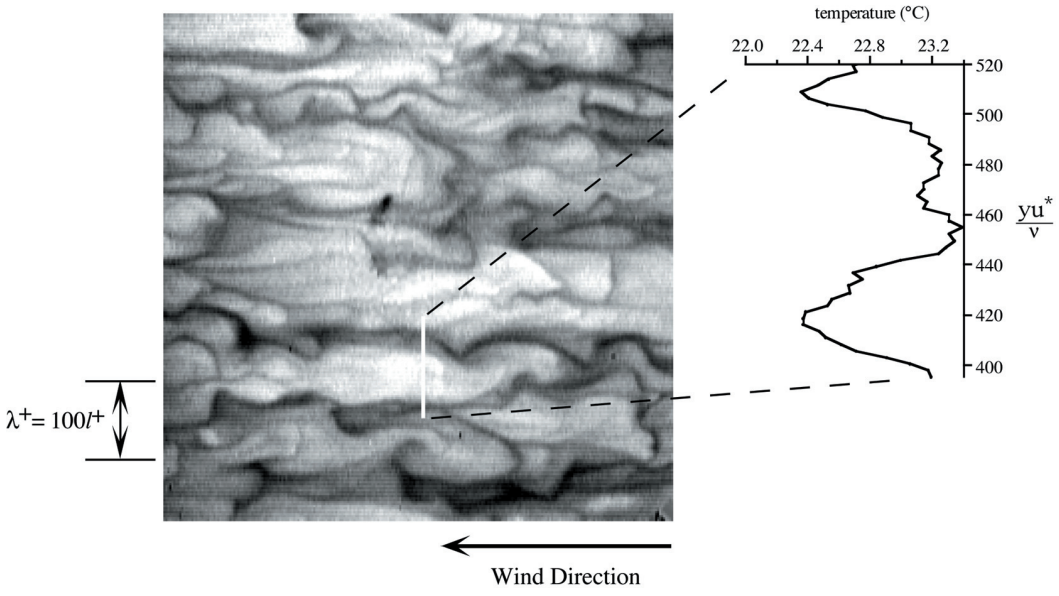

(a)

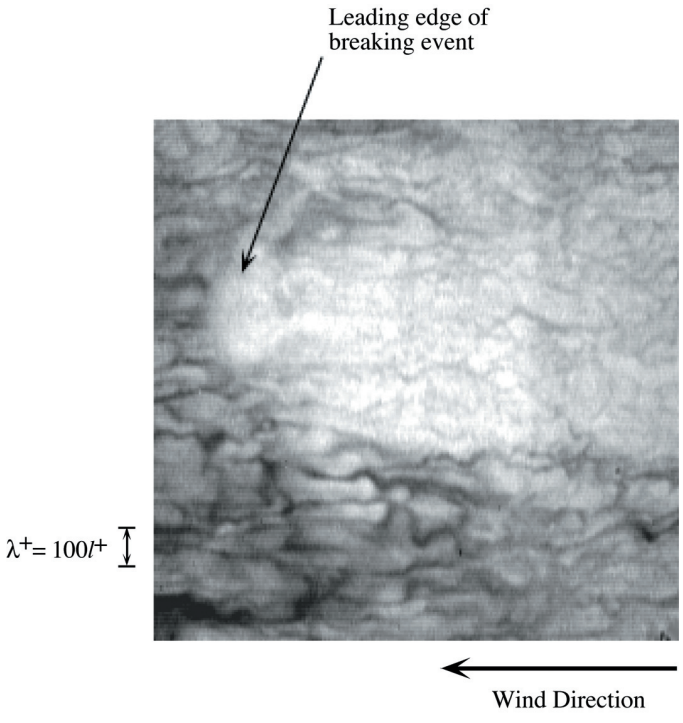

(b)

FIGURE 9

(a) IR image of a water surface at a wind speed of 2 ms^{-1} blowing from right to left. The image is 33 cm on a side. The light-colored areas are warm, rising plumes of water; the darker areas are cooler, descending sheets. The insert gives details of the temperature structure across a segment of the surface. Also indicated is the length scale $\lambda^+ = 100\ \lambda^+$. (b) IR image of the same surface at a wind speed of 4 ms^{-1}. The large, light-colored area is warmer water exposed by a small-scale breaking wave.